Check f

APPLIED SCIENCES AND ENGINEERING

Bulk photovoltaic effect and high mobility in the polar 2D semiconductor SnP₂Se₆

Vinod K. Sangwan¹†, Daniel G. Chica²†, Ting-Ching Chu³†, Matthew Cheng¹, Michael A. Quintero², Shiqiang Hao¹, Christopher E. Mead¹, Hyeonseon Choi¹, Rui Zu⁴, Jyoti Sheoran⁴, Jingyang He⁴, Yukun Liu¹, Eric Qian², Craig C. Laing², Min-A Kang¹, Venkatraman Gopalan⁴, Chris Wolverton¹, Vinayak P. Dravid¹, Lincoln J. Lauhon¹, Mark C. Hersam^{1,2,5}, Mercouri G. Kanatzidis²*

The growth of layered 2D compounds is a key ingredient in finding new phenomena in quantum materials, opto-electronics, and energy conversion. Here, we report SnP_2Se_6 , a van der Waals chiral (R3 space group) semiconductor with an indirect bandgap of 1.36 to 1.41 electron volts. Exfoliated SnP_2Se_6 flakes are integrated into high-performance field-effect transistors with electron mobilities $>100~cm^2/Vs$ and on/off ratios $>10^6$ at room temperature. Upon excitation at a wavelength of 515.6 nanometer, SnP_2Se_6 phototransistors show high gain ($>4 \times 10^4$) at low intensity ($\approx 10^{-6}~W/cm^2$) and fast photoresponse (<5~microsecond) with concurrent gain of ≈ 52.9 at high intensity ($\approx 56.6~mW/cm^2$) at a gate voltage of 60 V across 300-nm-thick SiO_2 dielectric layer. The combination of high carrier mobility and the non-centrosymmetric crystal structure results in a strong intrinsic bulk photovoltaic effect; under local excitation at normal incidence at 532 nm, short circuit currents exceed 8 mA/ cm^2 at 20.6 W/cm².

Copyright © 2024 me Authors, some rights reserved; exclusive licensee American Association for the Advancement of Science. No claim to original U.S. Government Works. Distributed under a Creative Commons Attribution NonCommercial

License 4.0 (CC BY-NC).

INTRODUCTION

The growing library of two-dimensional (2D) van der Waals (vdW) materials has played a central role in developing scalable and tunable electronics, optoelectronics, and nonlinear photonics. Monoelemental 2D materials are relatively rare, most of which are either semimetallic or unstable in ambient conditions (1, 2). Binary 2D compounds, such as transition metal dichalcogenides (TMDCs), represent a substantially larger class of vdW materials with a wide range of electronic and photonic properties (1, 3) that have used in a broad range of applications such as field-effect transistors (FETs), memtransistors, photodetectors, quantum technologies, and 2D magnetic switches (1, 2, 4, 5). Emerging electro-optical applications can exploit properties that arise from particular lattice symmetries, such as the bulk photovoltaic effect (BPVE) in non-centrosymmetric materials that produces photocurrent and photovoltage in the absence of a heterojunction or other geometrical asymmetries (Fig. 1, A and B) (6-8). Unlike the photoconductive effect, BPVE photocurrent does not require an external electric field, and unlike the photovoltaic effect, the BPVE photovoltage is not limited by the bandgap of the semiconductor. Although binary TMDCs can form non-centrosymmetric unit cells, the intrinsic polarity is weak (9, 10). Beyond TMDCs, layered ternary and quaternary compounds involving transition or posttransition metals provide greater variation in unit cell compositions and layer stacking permutations, which are expected to substantially broaden the technologically relevant scope for this class of materials (11, 12). Recently, researchers have observed unique electrical and optical properties in layered

¹Department of Materials Science and Engineering, Northwestern University, Evanston, IL 60208, USA. ²Department of Chemistry, Northwestern University, Evanston, IL 60208, USA. ³Applied Physics Graduate Program, Northwestern University, Evanston, IL 60208, USA. ⁴Department of Materials Science and Engineering, The Pennsylvania State University, University Park, PA 16802, USA. ⁵Department of Electrical Engineering and Computer Science, Northwestern University, Evanston, IL 60208, USA. *Corresponding author. Email: m-kanatzidis@northwestern.edu †These authors contributed equally to this work.

thiophosphate and selenophosphate crystals (13–15). Specifically, vdW crystals of metal chalcophosphates (e.g., thiophosphates and selenophosphates) can be exfoliated in few-layer sheets (16, 17) and are promising for electronic applications and high-energy radiation detection (18, 19). The chalcophosphates have at least three different elements with the stoichiometry of $M_2P_2Q_6$ (M = divalent metal, Q = S, Se) and AMP_2Q_6 (A = monovalent metals, M = trivalent metal) (20, 21). Thus, their great degree of functionality and tunability comes from distinct elements lending themselves to straightforward chemical manipulation. This family of vdW materials includes ferroelectric, magnetic, and half-metal materials; Mott insulators; nonlinear optical crystals; and semiconductors, with selenides having narrower bandgaps than sulfides (15–17, 21–28).

Here, we report the synthesis of a new layered chalcophosphate, SnP₂Se₆, using chemical vapor transport (CVT) and a P₂Se₅-based flux method. SnP₂Se₆ melts incongruently into Sn₂P₂Se₆ and a P/Se glass at \approx 408°C. SnP₂Se₆ adopts the chiral space group R3 [with lattice parameters a = b = 6.3213(9) Å and c = 19.962(4) Å] and is the first lamellar selenophosphate with a 4+ cation (29). Optical secondharmonic generation polarimetry revealed the non-centrosymmetric nature of SnP₂Se₆; and optical absorbance, photoluminescence, and photocurrent spectroscopy revealed an indirect bandgap in the range of 1.32 to 1.44 eV. Mechanically exfoliated SnP₂Se₆ flakes integrated into FETs showed n-type behavior with an electron field-effect mobility in the range of 55 to 113 cm²/Vs and an on/off ratio of $\approx 10^6$ at room temperature. SnP₂Se₆ phototransistors show a fast response time of less than 5 µs with responsivity exceeding 10⁵ A/W and detectivity exceeding 1014 Jones, making it the highest gain vdW phototransistor operating at this speed. We report BPVE originating from the non-centrosymmetric crystal structure of layered SnP₂Se₆; the spatially and angle-resolved photocurrent agrees qualitatively with a phenomenological shift current model. Local optical irradiation (wavelength of 532 nm) in the channel, away from the contacts, yields a large short-circuit current (I_{SC}) density of 8 mA/cm² that exceeds the intrinsic I_{SC} of ferroelectric insulators by one to three orders of magnitude (7-10, 30, 31).

RESULTS

Single-crystal x-ray diffraction (XRD) measurements were performed on the SnP₂Se₆ crystals synthesized by the CVT reaction. The compound crystallizes in the chiral space group R3 with lattice parameters a = b = 6.3213(9) Å and c = 19.962(4) Å. The refinement details, atomic coordinates, anisotropic displacement parameters, bond lengths, and bond angles are provided in tables S1 to S5. The layers are stacked in an ABCABC repeat sequence separated by vdW gaps (Fig. 1C), with the individual layers exhibiting the CdI₂ structure, in which Se occupies the I site, and Sn occupies the P₂ dumbbell, and a vacancy occupying the Cd sites (Fig. 1D). The coordination environment around the Sn⁴⁺ cation is a slightly distorted octahedron coordinated by Se, an environment similar to that of Sn⁴⁺ in SnSe₂.²⁶ The Sn-Se distances range from 2.710(3) to 2.717(3) Å in SnP₂Se₆ and are larger than those of octahedral Sn⁴⁺ centers in SnSe₂ [2.681(1) Å]. The P-P bond length is comparable to that of other layered selenophosphates (21). In addition, a residual electron density appears to be present in the empty octahedral site in the layer and the center of the P–P dimers, suggesting stacking faults.

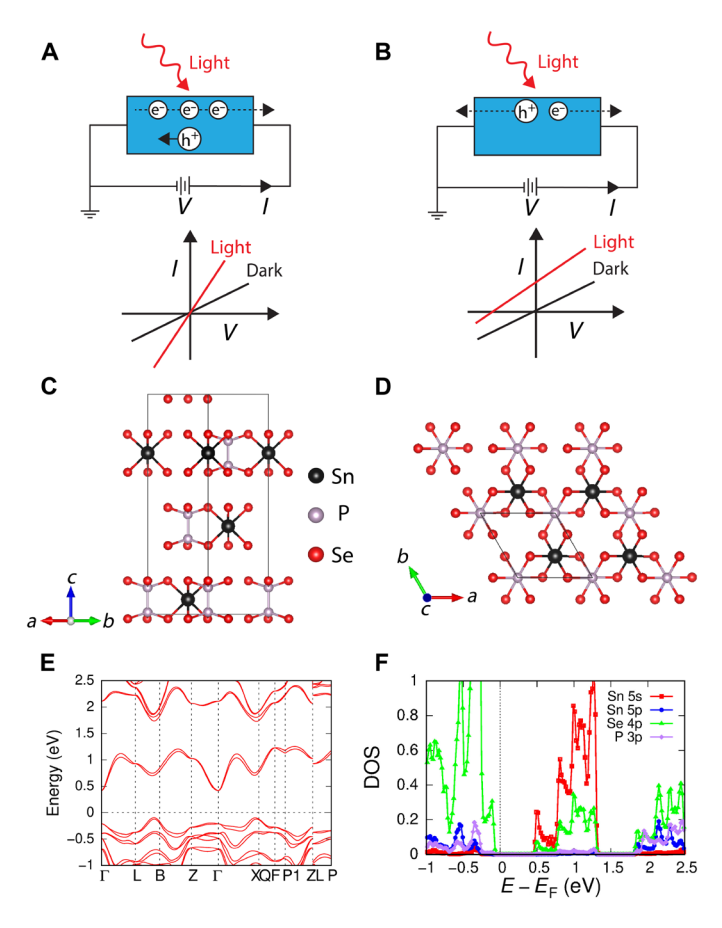


Fig. 1. Schematic of the BPVE mechanism, SnP_2Se_6 **crystal structure, and band structure.** (**A**) Schematic of photocurrent generation mechanism (top) and resulting current-voltage (*I-V*) characteristics (bottom) in a photoconductor. (**B**) Schematic of photocurrent generation from the BPVE (top) and resulting *I-V* characteristics (bottom) in a polar semiconductor. (**C** and **D**) Crystal structure of SnP_2Se_6 as viewed down the *ab* axis and the *c* axis, respectively. (**E**) Calculated band structure and (**F**) density of states (DOS) of SnP_2Se_6 with spin-orbit coupling calculated using the GGA approximation.

Density functional theory (DFT) band structure calculations suggest that SnP₂Se₆ is an indirect bandgap semiconductor with a conduction band minimum (CBM) at the Γ position and a valence band maximum (VBM) at a point along the L-B1 direction (Fig. 1E). The calculated indirect bandgap is approximately 0.55 eV, which is smaller than the experimental observations (1.32 to 1.44 eV) from three different measurements. The calculated bandgap is commonly underestimated because of an insufficient description of the electronic states when using the generalized gradient approximation (GGA). The spin-orbit coupling effect also plays a role in splitting the bands into double bands. The projected density of states in Fig. 1F shows that the VBM is dominated by the Se 4p states, shown as a green peak around -0.1 eV, and the CBM mainly originates from the Sn 5s state, as the red peak around 0.5 eV shows. The dimensional reduction from the bulk phase to monolayer thickness induces a symmetry change, and thus the Brillouin zones changed from rhombohedral for the bulk to hexagonal for the monolayer (fig. S4). The monolayer also exhibited an indirect bandgap with the VBM at the K point and CBM at the Γ point. In this case, the bandgap is enlarged to 0.84 eV compared to 0.55 eV for the bulk, albeit substantially smaller than the calculated bandgap of 2.23 eV for an SnP_2S_6 monolayer (28, 32, 33). The contributions to the VBM and CBM, as seen from the projected density of states for the monolayer, were similar to the bulk phase. In other words, the VBM and CBM consist mainly of Se 4p and Sn 5s orbitals, respectively.

Using DFT calculations, the density of states effective masses for electrons m_e^* and holes m_h^* were evaluated from $m_d^* = (g_2 m_{kx} m_{ky} m_{kz})^{1/3}$, resulting in values of 0.18 m_0 and 0.55 m_0 , respectively. For the electron, m_{kx} and m_{ky} were symmetrically equivalent at 0.09 m_0 , while m_{kz} was larger at 0.69 m_0 , corresponding to the crystal c direction. For the hole, the effective masses for m_{kx} and m_{ky} were approximately 0.37 m_0 , while m_{kz} was approximately 1.21 m_0 . Notably, the ratio of these effective masses in the in-plane and out-of-plane directions is larger than that of MoS₂, whereas the absolute value of the in-plane electron mass was lower than that of MoS₂ (0.47 m_0) (34).

Differential thermal analysis (DTA) measurements were performed on single crystals from the SnBr $_4$ CVT reaction as this reaction produces a single-phase material. Figure 2A shows the heat transfer as a function of temperature. During the first heating cycle, the onset of an endothermic event began at 408°C and peaked at 430°C. The remaining cooling and heating cycles did not show thermal events, indicating that SnP $_2$ Se $_6$ did not reform on cooling. PXRD after the DTA experiment showed that Sn $_2$ P $_2$ Se $_6$ was the only crystalline phase (fig. S5). Therefore, SnP $_2$ Se $_6$ melted incongruently at \approx 408°C, decomposing into Sn $_2$ P $_2$ Se $_6$ and P/Se glass. This relatively low melting point may explain why this compound has remained elusive because chalcophosphates are typically synthesized between 500° and 750°C.

Optical absorption spectroscopy performed on the SnP_2Se_6 crystals yielded an indirect optical bandgap of 1.32 eV (Fig. 2B). Diffuse reflectance measurements were also collected on lightly ground SnP_2Se_6 powder, which gave a similar optical bandgap of 1.36 eV (fig. S6), markedly redshifted compared to the sulfide analog (\approx 2.3 eV) (28, 35). Raman spectra confirmed the crystalline quality of the flakes that showed P_2Se_6 -like peaks at 217 and 447 cm⁻¹, in agreement with our previous report on 6LiInP_2Se_6 ; the peaks at 120 and 155 cm⁻¹ likely arise from Sn–Se bonds (Fig. 2C) (18). The room-temperature PL spectra (Fig. 2C inset) also showed a prominent peak at 836.3 nm (\approx 1.48 eV) that is accompanied by two side peaks

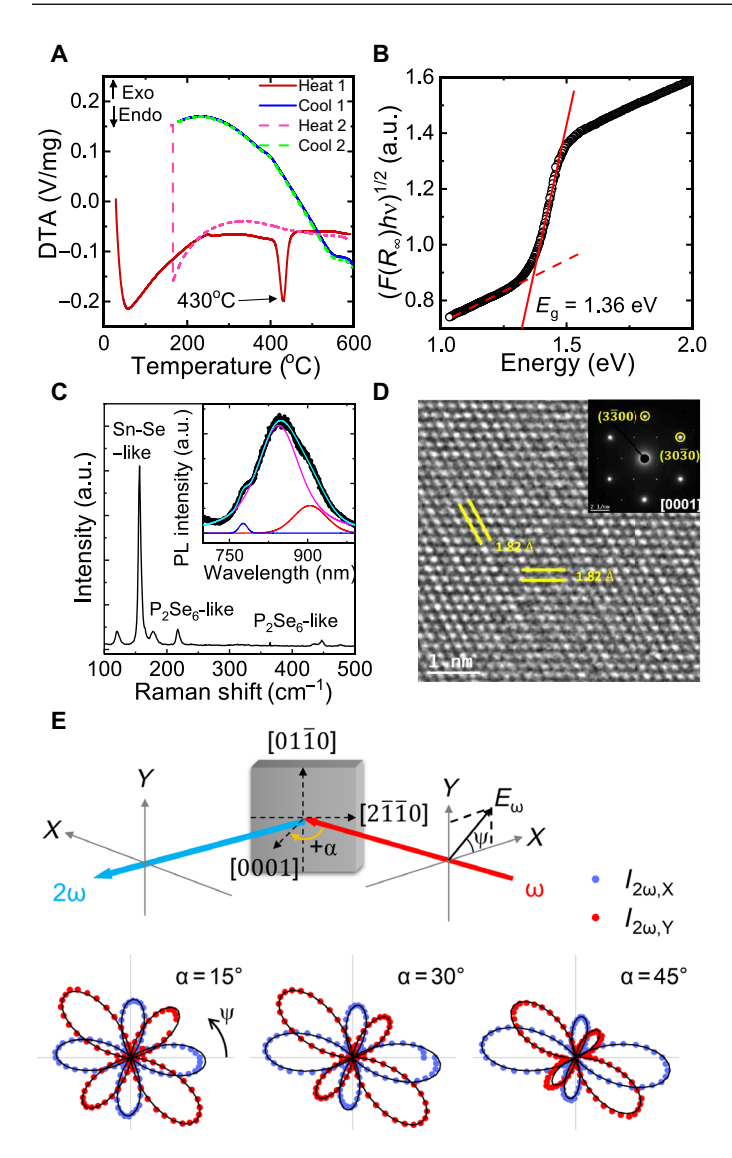


Fig. 2. Physical and optical properties of non-centrosymmetric SnP_2Se_6 bulk and exfoliated crystals. (A) Heat transfer versus temperature from a DTA experiment on a SnP_2Se_6 crystal grown by CVT. (B) Tauc plot to extract the indirect optical bandgap (1.36 eV) in a SnP_2Se_6 crystal. The optical transmission and photoemission yield spectra are shown in fig. S7. (C) Raman spectra from a SnP_2Se_6 flake using a 532-nm excitation. The inset shows photoluminescence spectra at the same excitation showing fits to three Voigt functions (see table S6 for fit parameters). (D) Highresolution transmission electron microscopy (HRTEM) image of a SnP_2Se_6 crystal showing a lattice spacing of 1.82 Å between ($\overline{3300}$) and ($\overline{3030}$) planes. Inset: Selected-area electron diffraction (SAED) showing the expected six-fold symmetry of a hexagonal system along the [0001]-zone axis (calculated SAED pattern is shown in fig. S9). (E) Experimental setup (top) and second harmonic generation (SHG) polar plots (bottom) of a SnP_2Se_6 crystal where the blue and red circles correspond to the SHG response collected along the lab X and lab Y directions, respectively. The black curves are the theoretical fits. a.u., arbitrary units.

at 1.39 and 1.59 eV (fig. S6C). Multiple photoluminescence peaks in indirect bandgap semiconductors could arise from shallow trap states, phonon-assisted processes, and multiple valleys in the band structure, as observed in indirect bandgap few-layer TMDC (36, 37). As discussed later, photocurrent spectroscopy further confirms the bandgap of SnP_2Se_6 flakes (thickness > 100 nm) mechanically

exfoliated from bulk crystals. Overall, the bandgap is found to be smaller than the bandgap of ultrathin SnP_2Se_6 flakes (2 to 16 layers) grown on mica by epitaxial growth (≈ 1.6 to 2 eV), likely due to quantum confinement and strain effects in the latter (38). Here, mechanical exfoliation was ineffective in obtaining ultrathin flakes approaching monolayer thicknesses. Last, the work function of SnP_2Se_6 was measured to be 5.72 eV based on the photoemission yield spectra (fig. S7B).

Transmission electron microscopy (TEM) bright-field images revealed the strain contrast in a representative flake due to the exfoliation process (fig. S8A). The selected-area electron diffraction (SAED) pattern taken perpendicular to the *ab* plane/along the *c* axis of SnP₂Se₆ showed nearly perfect sets of rotational symmetry patterns of a hexagonal crystal, indicating that the flake was highly single crystalline (inset of Fig. 2D). The c axis was parallel to the [0001]-zone axis, and a simulated SAED pattern of SnP₂Se₆ along the [0001]-zone axis (fig. S9) was in excellent agreement with the experimental SAED pattern. The high-resolution TEM (HRTEM) image in Fig. 2D shows the (3300)and (3030) lattice planes, and the corresponding larger view and a high-angle annular dark-field (HAADF) image of the same flake are shown in fig. S8 (A and B). The homogeneity of the local stoichiometry and chemical uniformity of the SnP₂Se₆ flakes were confirmed using energy dispersive x-ray spectroscopy (EDS) (fig. S8C). The stoichiometry of SnP₂Se₆ reasonably matched the expected value of 1:2:6 for Sn:P:Se, as shown in table S6, which, together with the SAED pattern, confirmed the formation of uniformly crystalline SnP₂Se₆.

To confirm that SnP_2Se_6 belonged to the polar space group R3 as opposed to $R\overline{3}$, we performed optical second harmonic generation (SHG) polarimetry. SHG is a second-order nonlinear optical process that is only exhibited in materials without inversion centers. The measurement combines two photons of frequency ω (wavelength = 800 nm) with a photon of frequency 2ω (wavelength = 400 nm). The experiment was conducted in reflection geometry at three different incident angles, α (Fig. 2E). The SHG intensities along the $[2\overline{110}]$ // lab X and $[0\overline{110}]$ // lab Y directions were collected as functions of the polarization angle ψ with respect to lab X. The six sets of polar plots were fitted to an analytical model (39) based on point group 3, as described in Methods. The excellent agreement between the theoretical fit and experiments confirms its non-centrosymmetric structure and point group 3 (Fig. 2E).

FETs were fabricated on mechanically exfoliated SnP₂Se₆ nanoflakes on 300-nm-thick SiO₂/Si substrates using a dry process inside an inert N2 glove box (Fig. 3A insets and figs. S10 to S12). The output characteristics of a typical FET measured in vacuum exhibited linear behavior at low biases, suggesting ohmic or quasiohmic contact with the Au electrodes (Fig. 3A). The transfer characteristics showed n-type semiconducting behavior with an electron field-effect mobility of 113 cm²/Vs (the range of 55 to 113 cm²/Vs is for 10 devices) and a switching ratio of 10⁶ (Fig. 3B). The FETs achieve an off-current of <1 nA [at drain voltage (V_D) of 5 V] with small values of threshold voltage $V_{\rm th}$ (<5 V), even at a channel thickness of 100 nm, suggesting weak intrinsic doping. The gate voltage (V_G) bias hysteresis is attributed to interfacial charge trapping. It should be noted that recent first-principles calculations of SnP₂Se₆ at room temperature predicted intrinsic electron and hole mobilities of 320 and 20 cm²/Vs, respectively, suggesting room for further mobility improvement by minimizing extrinsic disorder (33).

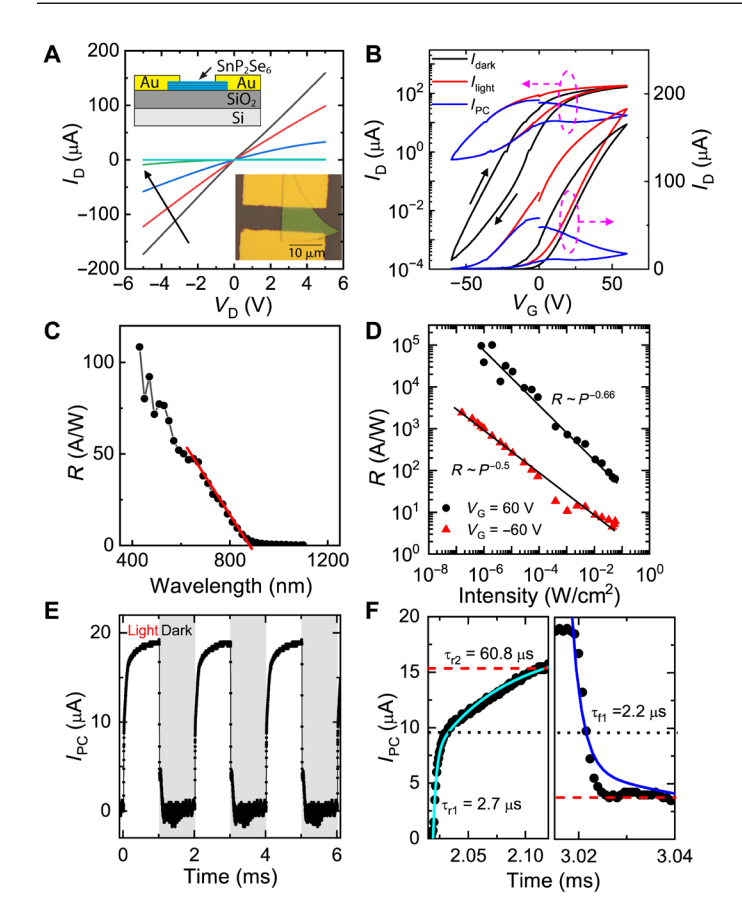


Fig. 3. Device characteristics of exfoliated SnP₂Se₆ FETs and phototransistors. (A) Output $(I_D - V_D)$ characteristics of the SnP_2Se_6 FET in the dark at varying gate voltage biases (V_G) from 60 to -60 V at steps of 20 V, as shown by the arrow. The top and bottom insets show a schematic and an optical image of the FET, respectively. (B) Transfer $(I_D - I_G)$ characteristics of a SnP₂Se₆ FET at $V_D = 5$ V in linear (right y axis) and log (left y axis) scales. I_D was measured in the dark (I_{dark}) and under illumination (I_{light}) at $\lambda = 515.6$ nm and $P = 56.6 \text{ mW/cm}^2$ to obtain $I_{PC} = I_{light} - I_{dark}$. Black arrows show the direction of the hysteresis loop. Linear transfer plots are also shown in fig. S13. (C) Responsivity $(R = I_{PC}/P, \text{ where } I_{PC} \text{ is photocurrent and } P \text{ is net illumination intensity}) \text{ of a } SnP_2Se_6$ phototransistor at $V_D = -1 \text{ V}$ and $V_G = 0 \text{ V}$ as a function of wavelength. The red line shows a linear fit intersecting the x axis at 880 nm (1.41 eV). (**D**) R versus P for $V_G = 60$ and -60 V (corresponding I_{PC} versus P is shown in fig. S14). (**E**) Time-resolved I_{PC} while the illumination is turned on (rise) and off (fall) at a frequency of 500 Hz at $V_G = 60$ V, $V_D = 2$ V, and $P = 56.6 \text{ mW/cm}^2$. (F) Transient I_{PC} near illumination turn on and off is fit to multiexponential functions with two and one characteristic time constants for rise (τ_{r1} and τ_{r2}) and fall (τ_{f1}) shown in left and right zoomed-in plots, respectively. See figs. S15 to S17 for full exponential fits as a function of frequency. Red dashed lines show 80 and 20% levels of the photocurrent in the left and right plots, respectively. The black dashed line shows 50% level of the photocurrent.

The spectrally resolved photocurrent in the SnP₂Se₆ phototransistor reveals a bandgap of 1.41 eV (Fig. 3C), in agreement with the optical absorbance and PL spectra (Fig. 2, B and C). Transfer characteristics under illumination (wavelength = 515.6 nm; intensity, $P=56.6~\rm mW/cm^2$) show that photogenerated excess carriers increased the net current ($I_{\rm light}$) by more than 1000-fold in depletion ($V_{\rm G}=-60~\rm V$) but only by 20% in accumulation ($V_{\rm G}=60~\rm V$), as expected by trap filling in accumulation (Fig. 3B) (40). The photocurrent ($I_{\rm PC}=I_{\rm light}-I_{\rm dark}$, where $I_{\rm dark}$ is dark current) and photoresponsivity ($R=I_{\rm PC}/P$) show power-law behaviors of $I_{\rm PC}\sim P^{1-m}$ (fig. S14)

and $R \sim P^m$, respectively, with the exponent m changing with V_G (41). For example, R varies as $\sim P^{0.66}$ and $\sim P^{0.5}$ for gate bias values of $V_G = 60$ and -60 V, respectively (Fig. 3D). The power-law exponent of 0.5 in depletion and deviations from it in accumulation is evidence of bimolecular recombination as expected in phototransistors (40, 42). The photoresponsivity approaches 10^5 A/W (gain >4.2 × 10^4) at low intensities (<1 μ W/cm²) at $V_G = 60$ V, comparable to the highest reported values for layered semiconductors (Fig. 3D) (41, 42). Detectivity (D) is estimated by $D = R(A)^{0.5}/I_N$ where A is area and I_N is dark noise current. Assuming shot noise [i.e., $I_N = (2eI_{\rm dark})^{0.5}$] being dominant at $V_G = -60$ V, we obtain $D = 1.7 \times 10^{14}$ Jones.

The temporal response of photocurrent was recorded in an oscilloscope while modulating the light at different frequencies (f) ranging from 100 Hz to 5 kHz (Fig. 3E and fig. S15) At low-frequency f < 2 kHz, transient I_{PC} at the onset of illumination was fit to a multi-exponential function with three characteristics rise times (τ_{r1} , τ_{r2} , and τ_{r3}), $I_{PC} = A - B. \exp \left[-(t - t_0) / \tau_{r1} \right] - C. \exp \left[-(t - t_0) / \tau_{r2} \right] - D. \exp \left[-(t - t_0) / \tau_{r3} \right]$ to obtain $\tau_{\rm rl} \approx 2.7$ µs, $\tau_{\rm r2} \approx 60.8$ µs, and $\tau_{\rm r3} \approx 532$ µs (Fig. 3, F and G, and fig. S16). At high-frequency f > 2 kHz, transient I_{PC} rise can fit to a biexponential function with τ_{r1} and τ_{r2} since τ_{r3} approaches 1/f. For practical purposes, the response time of photodetectors is typically defined in two ways: the time required to change the photocurrent by 80% and by 50% (42). Here, I_{PC} rises by 50% in 9.5 µs and by 80% in 105 μ s. On the other hand, decrease in I_{PC} in dark can fit to a biexponential function, $I_{PC} = E + F \cdot \exp\left[-(t-t_0)/\tau_{f_1}\right] + G \cdot \exp\left[-(t-t_0)/\tau_{f_2}\right]$ to obtain characteristic fall times $\tau_{\rm fl} \approx 2.2~\mu s$ and $\tau_{\rm fl} \approx 50.6~\mu s$ (Fig. 3, F and H, and fig. S17). Transient I_{PC} decays by 50% in 2.5 μ s and by 80% in 5.2 µs. The 3-dB bandwidth of the photodetectors, defined by the modulation frequency to achieve 50% of the dc photocurrent (19 μ A at $V_D = 2$ V), is limited by rise photocurrent, giving a value of ≈ 105 kHz (≈ 400 kHz for the decay). Note that both τ_{r1} and τ_{f1} remain relatively unchanged at all frequencies in the range of 100 Hz to 5 kHz (figs. S16 and S17) and approach the instrumentation resolution of ≈ 3 µs. We emphasize the importance of concurrent measurements of gain and speed, and at these conditions ($V_G = 60 \text{ V}$, $V_D = 2 \text{ V}$, and $P = 56.6 \text{ mW/cm}^2$), we get a gain of 212, resulting in a gain bandwidth product of ≈22.3 MHz. The photocurrent power and gate voltage dependencies suggest a trap-assisted internal gain mechanism with gain $\sim \tau_{eff}/\tau_{tr}$, where τ_{tr} is transit time and τ_{eff} is effective lifetime of photocarriers obtained from $\tau_{eff} = \tau_r (\tau_d/\tau_t)$ using recombination time (τ_r), detrapping time (τ_d), and trapping time (τ_t) (40). We obtain $\tau_{tr} = 2.1$ ns from $\tau_{tr} = L^2/(\mu V_D)$ where L and μ are channel length and electron mobility, respectively (40). Using a gain of 212 (or 3-dB gain of 106) at $V_{\rm D}=2$ V, we get $\tau_{\rm eff}\approx 444$ ns (\approx 222 ns), which is roughly 5 to 10 times smaller than measured time constants τ_{r1} and τ_{f1} (Fig. 3F), suggesting a faster intrinsic response that is below the instrumentation resolution. Different rise and fall times are common in semiconductors due to the asymmetric kinetics of trapping and detrapping processes (40). Overall, the combination of metrics, gain, detectivity, and speed of SnP₂Se₆ phototransistors compare favorably with the state of the art in 2D materials (41) and outperform metrics from a recent report on SnP₂Se₆ by at least two orders of magnitude (38).

 SnP_2Se_6 exhibits an open-circuit voltage (V_{OC}) and a short-circuit photocurrent whose spatial and polarization dependence indicates the presence of a BPVE (Fig. 4). Photogating was eliminated as a source of photocurrent by fabricating devices on quartz substrates, with the

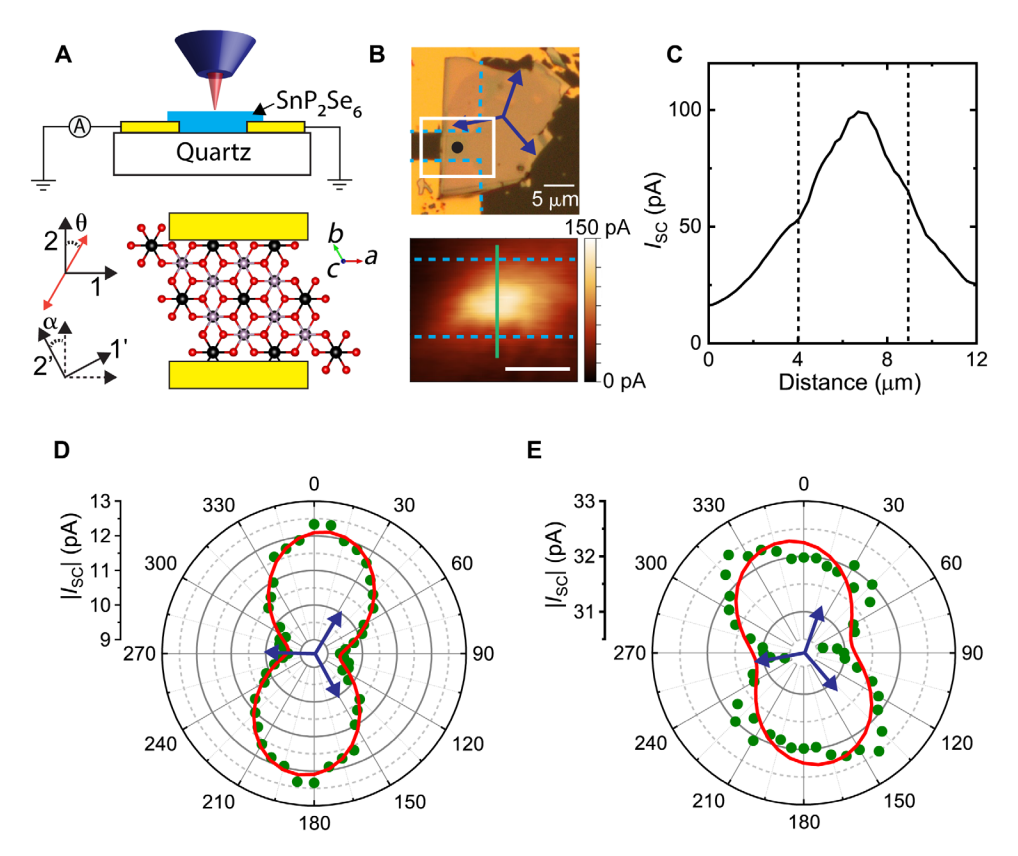


Fig. 4. Photocurrent measurements of intrinsic BPVE in two-probe exfoliated SnP₂Se₆ devices. (**A**) Top: Side-view schematic of a bottom-contacted SnP₂Se₆ device on a quartz substrate under photoexcitation. Bottom: Top-view schematic of the SnP₂Se₆ device where 1 and 2 denote the axes aligned with the low-index axis and the channel, respectively. θ is the angle between the linear polarized light direction and axis 2 that is aligned parallel to the channel direction (perpendicular to electrode edges). α is the angle between axis 2 and the channel direction in an arbitrary device. Symmetry axes (a, b, and c) and color scheme of atoms are the same as Fig. 1 (C and D). (**B**) Top: An optical micrograph of a typical device. Blue dashed lines denote the electrode edges; blue arrows show the equivalent direction "a" in a threefold crystal symmetry, as determined by EBSD. Bottom: Spatially resolved zero-voltage photocurrent (l_{SC}) map of the device from the area indicated by the white rectangle in the top image. An excitation wavelength of 532 nm was used at an intensity of 2.8 W/cm². Scale bars, 5 μm (top) 3 μm (bottom). (**C**) Line profiles of l_{SC} along the green line in the photocurrent map in (B). The dashed lines denote the contact edges. (**D** and **E**) Angle-resolved l_{SC} for two devices using an intensity of 12.2 and 2.8 W/cm², respectively. Error bars are shown in fig. S20. Red lines are fits to a phenomenological model for BPVE discussed in the text.

source electrode grounded and the short circuit current I_{SC} measured at the drain electrode; the current preamplifier acts as a virtual ground (Fig. 4A and see also Methods). Note that SnP₂Se₆ was found to react with common solvents used in photolithography; thus, these devices were fabricated by mechanically exfoliating SnP₂Se₆ flakes directly on prepatterned electrodes on quartz to avoid exposure to any chemicals. The crystal orientation was determined by electron backscatter diffraction (EBSD) (fig. S18) following electrical measurements. Two features of the short-circuit photocurrent observed in multiple devices are consistent with a BPVE in SnP₂Se₆. First, the spatially resolved I_{SC} with above-gap excitation (wavelength of 532 nm, spot diameter ≈1.3 µm) exhibits a maximum near the center of the channel (Fig. 4, B and C). Second, I_{SC} depends on the polarization of the incident light, as shown in Fig. 4 (D and E), with 0° corresponding to polarization along axis 2, parallel to the channel (Fig. 4A). The symmetry of the polarizationdependent photocurrent is analyzed below after first considering alternatives to the BPVE.

The absence of spatially localized photocurrent at the contacts (Fig. 4, B and C) rules out the dominance of a Schottky barrier photovoltaic effect (9, 10, 43) and photothermoelectric currents arising from the differences in the temperature and Seebeck coefficients of

the semiconductor and metal contacts (44). BPVE from ferroelectric domains is not expected from R3 space group, and indeed, piezo-force microscopy (PFM) conducted in two different systems (see Methods) shows no hysteretic response within a voltage range of -2 to 2 V (figs. S24 to S27). Spatially resolved SHG of similar SnP₂Se₆ devices on Si wafers revealed a single polar domain throughout the whole flake, thus ruling out stacking faults, edge-embedded vdW heterostructures, and flexophotovoltaic effect from residual strain (figs. S19 and S28 to S34) (45, 46). Last, the Shockley-Ramo effect is not expected to contribute due to weak Coulomb interactions between carriers and the high intrinsic resistivity in comparison to materials in which it has been observed (47).

The expected angle dependence of the I_{SC} arising from a BPVE can be derived from a phenomenological model based on the piezo-electric coefficients d_{11} and d_{22} , as described in the Supplementary Materials (48). Briefly, the polarization angle-dependent photocurrent (J_i) can be calculated using

$$J_{i} = \sigma d_{ijk} E_{ij} E_{k} \tag{1}$$

where σ is the electrical conductivity, d_{ijk} is the converse piezoelectric coefficient, and E_i and E_k denote orthogonal components of the

electric field. For simplicity, we assume that σ is isotropic in the 2D plane because effective masses $m_{\rm kx}$ and $m_{\rm ky}$ are nearly identical. We designate axes 1 and 2 as parallel and perpendicular to contact edges, respectively (Fig. 4A); only J_2 contributes to the photocurrent collected by the contacts. For the crystal orientation shown in Fig. 4A, the photocurrent varies with the angle of polarization θ as $\sim (d_{22} \cos 2\theta - d_{11} \sin 2\theta)$. For a device in which the crystal is rotated by an angle α with respect to edges of electrodes, the expression becomes

$$J_2'(\theta) = \text{const.} * \left[d_{22} \cos(2\theta + 3\alpha) - d_{11} \sin(2\theta + 3\alpha) \right] + C$$
 (2)

where C is a polarization-independent background current. The expected angle (θ) dependence of photocurrent is shown in fig. S35 for the case of $\alpha = 0$ and selected values of d_{11} and d_{22} . Because α was determined by EBSD, the experimental data in Fig. 4 (D and E) can be fit using Eq. 2 with d_{11} and d_{22} as fitting parameters that determine the polarization dependence. The devices in Fig. 4 (D and E) show similar d_{11}/d_{22} ratios of 4.1 and 5.7, respectively. For comparison, SnP₂S₆, which belongs to the same crystal symmetry, shows $d_{11}/d_{22} > 10$ (28).

Last, we attribute the angle-independent background I_{SC} (C) to the asymmetric diffusion of photogenerated carriers due to the Dember effect (8, 10, 49). The Dember effect may arise from asymmetric optical illumination or intrinsic inhomogeneities in a material, such as thickness variations in SnP₂Se₆ flakes, resulting in spatially separated electrons and holes that increase the recombination lifetime and improve collection efficiency (50). We do not expect asymmetric carrier diffusion to correlate with underlying crystal symmetry because DFT calculations, discussed above, suggest equal in-plane effective electron masses ($m_{\rm kx}$ and $m_{\rm ky}$) in x and y directions. Thus, we also do not expect in-plane anisotropy in charge carrier mobility. Subtraction of C from the net photocurrent shows a reversal of the sign of $V_{\rm OC}$ and $I_{\rm SC}$ in all measured devices (fig. S21).

Overall, SnP₂Se₆ shows a maximum photocurrent density of 8.87 mA/cm² at 20.6 W/cm² that is one to three orders of magnitude larger (at the same intensity) than single-domain noncentrosymmetric materials with intrinsic BPVE such as Pb[Zr,Ti] O_3 , BaTi O_3 , BiFe O_3 , and [CH₃NH₃]PbI₃, etc. (30, 51, 52) Similar I_{SC} values were also measured on SnP₂Se₆ phototransistors on Si (figs. S22 and S23). A comprehensive comparison plot in fig. S36 shows that the BPVE I_{SC} density at different illumination intensities for SnP₂Se₆ is higher or comparable to that of layered ferroelectric α-In₂Se₃ and vertical graphene/CuInP₂S₆/graphene devices (53, 54). Note that a larger BPVE photocurrent density has previously been observed in ferroelectric materials with multiple domain walls that are engineered to achieve large I_{SC} and V_{OC} (52). A non-polar, non-centrosymmetric crystal can also produce BPVE when the polarization aligns with high-symmetry axes (6), but resulting photocurrent is expected to increase in systems with inherent polarization within the unit cell in Dirac-like materials (8) and in engineered systems with additional symmetry breaking such as nanotubes (6, 9, 10). However, the photocurrent density is one to two orders of magnitude smaller than materials with engineered polar symmetry such as WS2 nanotubes and WSe₂-black phosphorus heterojunction, and similar strategies can be potentially applied to SnP₂Se₆ to further enhance BPVE (9, 10). For practical applications, global uniform illumination could also be used to enhance net I_{SC} and V_{OC} by using symmetric and ohmic contacts.

DISCUSSION

Semiconducting SnP₂Se₆ crystals has been grown in a layered, chiral structure with high crystallinity and nanoscale homogeneity and an indirect bandgap of 1.36 eV. SnP₂Se₆ nanoflake (photo)transistors showed high room-temperature electron mobilities (>100 cm²/Vs), switching ratios (>10⁶), a fast photoresponse (\approx 3 μ s), large detectivity (>10¹⁴ Jones), and responsivities (\approx 10⁵ A/W) that are expected to improve further in scaled devices. The combination of high mobility and spontaneous polarization yields a strong intrinsic BPVE with photocurrent density (8 mA/cm² at 20.6 W/cm²) outperforming single-domain ferroelectric insulators. Thus, this work lays the groundwork for further exploring ternary selenophosphates for high-performance electronic and optoelectronics.

METHODS

SnP₂Se₆ synthesis

The following reagents were used as received: tin shot (99.999%; American Elements), phosphorus chunk (99.999%; Puratronic), selenium shot (99.999%; Puratronic), tin (IV) bromide (99%; Sigma-Aldrich), and iodine (99.999%; Sigma-Aldrich). Phosphorus (1.3563 g, 43.8 mmol) and selenium (8.6437 g, 109.5 mmol) were loaded into a fused silica tube with inner and outer diameters (i.d. and o.d.) of 10.5 and 12.7 mm, respectively, and then sealed to a pressure of 3×10^{-3} mbar with an oxy/natural gas torch. The tube was loaded into a computer-controlled furnace and then set to the following heating profile: heated to 500°C for 24 hours, soaked for 96 hours, and cooled down to room temperature for 12 hours.

For flux synthesis method 1, tin (0.0305 g, 0.257 mmol) and P_2Se_5 (0.4695 g, 1.03 mmol) were loaded into a 12.7-mm-o.d. and 10.5-mm-i.d. fused silica tube and then sealed to a pressure of 3×10^{-3} mbar with an oxy/natural gas torch. The tube was placed in a computer-controlled furnace and subjected to the following profile: heated to 500°C for 24 hours, soaked for 36 hours, cooled to 250°C for 50 hours, and then cooled down to room temperature.

For flux synthesis method 2, tin (0.5750 g, 4.84 mmol) and P_2Se_5 (4.4250 g, 9.69 mmol) were loaded into a 12.7-mm-o.d, and 10.5-mm-i.d. fused silica tube and then sealed to a pressure of 3×10^{-3} mbar with an oxy/natural gas torch. The tube was placed in a computer-controlled furnace and subjected to the following profile: heated to 375°C for 6 hours, soaked for 6 days, and then cooled to room temperature for 6 hours.

For CVT synthesis, tin (0.3628 g, 3.06 mmol), phosphorus (0.1893 g, 6.11 mmol), selenium (1.4479 g, 18.3 mmol), and SnBr₄ (0.020 g, 0.046 mmol) were loaded into an 18-mm-o.d, and 16-mm-i.d. fused silica tube and then sealed to a pressure of 3×10^{-3} mbar with an oxy/natural gas torch. The tube was placed in a two-zone computer-controlled tube furnace and subjected to the following heating profile: source side: heated to 450°C for 24 hours, soaked for 144 hours, and then cooled down to room temperature for 10 hours and sink side: heated to 325°C for 24 hours, soaked for 144 hours, and cooled down to room temperature for 10 hours. The source and sink sides were where the reagents were placed, and the SnP₂Se₆ crystals were deposited, respectively.

X-ray diffraction

Powder XRD (PXRD) patterns were collected on lightly ground samples using a Miniflex 600 powder x-ray diffractometer with a Cu x-ray source and graphite monochromator (fig. S1). The sample

holder was a zero-background silicon holder. The calculated powder patterns were obtained using the Mercury software from reference. cif files (55). The single-crystal XRD pattern was collected on a CVT-grown SnP₂Se₆ crystal using a STADI VARI diffractometer equipped with an Ag source and a CdTe detector. The temperature was maintained at 293 K using an Oxford cryosystem low-temperature device. Data reduction was achieved using the x-area software suite, X-Area (STOE & Cie, Darmstadt, Germany, 2002). The structure solution was obtained using olex2.solve with charge flipping (56). The graphical user interface was olex2 (56). ShelXL (57) was used to refine the model using least-squares minimization.

Device fabrication and electrical and photocurrent measurements

SnP₂Se₆ transistors were fabricated by evaporating 70-nm-thick Au electrodes through TEM grid masks (holes, 30 µm by 30 µm by 7 µm) in an inert N₂ glove box. Only well-defined rectangular or trapezoidal SnP₂Se₆ flakes on 300-nm-SiO₂/Si wafers were selected for electrical and photocurrent measurements. For BPVE, bottom contact SnP₂Se₆ devices were fabricated on quartz substrate by first patterning source/drain electrodes (50-nm Au on 3-nm Cr) by photolithography, followed by mechanically exfoliating SnP₂Se₆ flakes. All electrical measurements of the SnP₂Se₆ transistors were conducted using a Keithley Source Meter 2400 unit and a cryoprobe station (Lakeshore CRX-4 K) at a base pressure of 5 × 10⁻⁵ torr using protocols described earlier (41).

Photocurrent measurements

Voltage bias-dependent, intensity-dependent, and time-resolved photocurrent measurements (Fig. 3) of SnP_2Se_6 phototransistors were conducted in the probe station (Lakeshore CRX-4 K) using a fiber-coupled laser diode (LP520MF100) at 515.6 nm while modulating the output optical power using a Thor Labs TEC controller (ITC4001) using the setup described previously in (41). Time-resolved measurements were done by converting the drain current to a voltage by a preamplifier (DL Instruments, Ithaco 1211) while modulating the light output (ITC4001) in square waves using an external waveform generator (Agilent 33500B), and resulting time traces were captured by an oscilloscope (Tek MDO4000C).

The spectrally resolved and angle-resolved zero-bias BPVE photocurrent was measured using a confocal microscope (WiTec System) coupled with a tunable coherent white light source (NKT Photonics). The photocurrent was converted into voltage using a current preamplifier (DL Instruments, Ithaco 1211) and recorded using a lock-in amplifier (Signal Recovery Model 7265), while the light was modulated at a frequency of 2137 Hz. For spectrally resolved photocurrent, the whole device channel was illuminated by using a 20× objective. For spatially resolved photocurrent, the laser was focused on a spot (diameter = $1.3 \mu m$) using a long working distance 50× objective (numerical aperture = 0.5) to produce 2D photocurrent maps. The device electrodes were contacted with two microprobes resting on a piezo stage. For I_{SC} measurements, the drain and source electrodes were connected to the ground and the virtual ground of the preamplifier, respectively. $V_{\rm OC}$ was extracted from current-voltage characteristics obtained by the lock-in amplifier. The current noise floor of the measurement setup was estimated to be ≈500 fA. Lock-in measurements of the device with lifted probes revealed a built-in voltage of less than 1 mV. The measured angle-resolved photocurrent was normalized by the power measured

at the sample plane while rotating the polarizer to account for variations in the reflectivity of the beam splitter (fig. S19). The polarization angle dependence of the short circuit photocurrent is described by a phenomenological model of the BPVE in the Supplementary Materials.

Electron backscatter diffraction

EBSD data were collected using an FEI Quanta 650 with Oxford Instruments aZtec EBSD system at an accelerating voltage of 10 kV. The collected patterns were indexed using the Oxford Instruments AZtec commercial software associated with the instrument. A custom structure file containing the atomic positions and symmetry was used to generate the simulated Kikuchi patterns for indexing.

Piezo-force microscopy

PFM was conducted on a commercial SPM system (Bruker Dimension Icon) with Pt/Ir-coated AFM tips (Nanosensors, PPP-EFM) under ambient conditions. PFM images were measured with a drive frequency of \approx 360 kHz, which is near the contact resonance frequency (CRF) of the flexural mode, and a drive amplitude of 1.5 V. For out-of-plane dc bias sweeps, PFM responses were measured at discrete points on the sample at the same drive frequency and amplitude at dc bias offsets ranging from -2 to 2 V.

PFM measurements were also repeated on an Asylum Cypher AFM system using Pt/Ir-coated tips (Nanosensors, PPP-EFM) that produced a PFM signal with a larger signal-to-noise ratio than the Bruker system. Dual ac resonance tracking–PFM measurements were performed to obtain image scans of the piezoresponse. Switching spectroscopy–PFM was used to perform dc bias sweeps. For out-of-plane PFM measurements, the tip was driven at a drive frequency of \approx 320 kHz near the CRF of the flexural mode with a drive amplitude of 1.25 V. For in-plane PFM measurements, the tip was driven at a drive frequency of \approx 650 kHz near the CRF of the torsional mode with a drive amplitude of 2 V.

Optical SHG polarimetry

Optical SHG polarimetry was performed in the reflection geometry at 800 nm at three incident angles: $\alpha = 15^\circ$, 30° , and 45° , as shown in Fig. 2E. The incident beam was generated using a Ti:sapphire femtosecond laser system (100 fs, 1 kHz). The crystal was oriented such that $[2\overline{110}]$ // lab X, $[01\overline{10}]$ // lab Y, and [0001] // lab Z. During the measurement, the incident beam was linearly polarized and rotated by an angle ψ with respect to the lab X direction. The SHG intensities were decomposed into lab X and lab Y directions using an analyzer and collected by a photomultiplier tube detector. The polar plots were fitted simultaneously using an analytical model (39) based on point group 3, whose nonlinear polarization can be written as

$$\begin{bmatrix} P_{\mathbf{x}}^{2\omega} \\ P_{\mathbf{y}}^{2\omega} \\ P_{\mathbf{z}}^{2\omega} \end{bmatrix} = \begin{bmatrix} d_{11} & -d_{11} & 0 & d_{14} & d_{15} & -d_{22} \\ -d_{22} & d_{22} & 0 & d_{15} & -d_{14} & -d_{11} \\ d_{31} & d_{31} & d_{33} & 0 & 0 & 0 \end{bmatrix} \begin{bmatrix} (E_{\mathbf{x}}^{\omega})^{2} \\ (E_{\mathbf{y}}^{\omega})^{2} \\ (E_{\mathbf{y}}^{\omega})^{2} \\ 2E_{\mathbf{y}}^{\omega} E_{\mathbf{z}}^{\omega} \\ 2E_{\mathbf{x}}^{\omega} E_{\mathbf{y}}^{\omega} \end{bmatrix}$$
(3)

The SHG intensity, $I^{2\omega} \propto |P^{2\omega}|^2$, can be expressed as

$$\begin{split} &I_{2\omega,X} \propto \left| \cos(\alpha) [d_{11}\cos(\alpha)^2 \cos(\psi)^2 - d_{15}\cos(\psi)^2 \sin(2\alpha) \right. \\ &- d_{22}\cos(\psi)\sin(2\psi) - d_{14}\sin(\alpha)\sin(2\psi) - d_{11}\sin(\psi)^2] \\ &- \sin(\alpha) [d_{31}\cos(\alpha)^2 \cos(\psi)^2 + d_{33}\cos(\psi)^2 \sin(\alpha)^2 + d_{31}\sin(\psi)^2] \right|^2 \end{split}$$

$$I_{2\omega,Y} \propto \left| -d_{22}\cos(\alpha)^2 \cos(\psi)^2 + d_{14}\cos(\psi)^2 \sin(2\alpha) - d_{11}\cos(\alpha)\sin(2\psi) - d_{15}\sin(\alpha)\sin(2\psi) + d_{22}\sin(\psi)^2 \right|^2$$

Supplementary Materials

This PDF file includes:

Supplementary Text Figs. S1 to S36 Tables S1 to S7 References

REFERENCES AND NOTES

- V. K. Sangwan, M. C. Hersam, Electronic transport in two-dimensional materials. Annu. Rev. Phys. Chem. 69, 299–325 (2018).
- D. Jariwala, V. K. Sangwan, L. J. Lauhon, T. J. Marks, M. C. Hersam, Emerging device applications for semiconducting two-dimensional transition metal dichalcogenides. ACS Nano 8. 1102–1120 (2014).
- S. Haastrup, M. Strange, M. Pandey, T. Deilmann, P. S. Schmidt, N. F. Hinsche, M. N. Gjerding, D. Torelli, P. M. Larsen, A. C. Riis-Jensen, J. Gath, K. W. Jacobsen, J. Jørgen Mortensen, T. Olsen, K. S. Thygesen, The computational 2D materials database: High-throughput modeling and discovery of atomically thin crystals. 2D Mater. 5, 042002 (2018).
- K. F. Mak, J. Shan, Photonics and optoelectronics of 2D semiconductor transition metal dichalcogenides. Nat. Photonics 10, 216–226 (2016).
- X. Yan, J. H. Qian, V. K. Sangwan, M. C. Hersam, Progress and challenges for memtransistors in neuromorphic circuits and systems. *Adv. Mater.* 34, e2108025 (2022).
- V. M. Fridkin, Bulk photovoltaic effect in noncentrosymmetric crystals. Crystallogr. Rep. 46, 654–658 (2001).
- L. Z. Tan, A. M. Rappe, Upper limit on shift current generation in extended systems. Phys. Rev. B 100, 085102 (2019).
- 8. A. M. Cook, B. M. Fregoso, F. de Juan, S. Coh, J. E. Moore, Design principles for shift current photovoltaics. *Nat. Commun.* **8**, 14176 (2017).
- T. Akamatsu, T. Ideue, L. Zhou, Y. Dong, S. Kitamura, M. Yoshii, D. Yang, M. Onga, Y. Nakagawa, K. Watanabe, T. Taniguchi, J. Laurienzo, J. Huang, Z. Ye, T. Morimoto, H. Yuan, Y. Iwasa, A van der Waals interface that creates in-plane polarization and a spontaneous photovoltaic effect. *Science* 372, 68–72 (2021).
- Y. J. Zhang, T. Ideue, M. Onga, F. Qin, R. Suzuki, A. Zak, R. Tenne, J. H. Smet, Y. Iwasa, Enhanced intrinsic photovoltaic effect in tungsten disulfide nanotubes. *Nature* 570, 349–353 (2019).
- J. Yao, G. Yang, Multielement 2D layered material photodetectors. Nanotechnology 32, 392001 (2021).
- M. A. McGuire, Cleavable magnetic materials from van der Waals layered transition metal halides and chalcogenides. J. Appl. Phys. 128, 110901 (2020).
- B. L. Chittari, Y. Park, D. Lee, M. Han, A. H. MacDonald, E. Hwang, J. Jung, Electronic and magnetic properties of single-layer MPX₃ metal phosphorous trichalcogenides. *Phys. Rev.* B 94, 184428 (2016).
- R. Samal, G. Sanyal, B. Chakraborty, C. S. Rout, Two-dimensional transition metal phosphorous trichalcogenides (MPX₃): A review on emerging trends, current state and future perspectives. *J. Mater. Chem. A* 9, 2560–2591 (2021).
- F. M. Wang, T. A. Shifa, P. Yu, P. He, Y. Liu, F. Wang, Z. X. Wang, X. Y. Zhan, X. D. Lou, F. Xia, J. He, New frontiers on van der Waals layered metal phosphorous trichalcogenides. *Adv. Funct. Mater.* 28, 1802151 (2018).
- R. N. Jenjeti, R. Kumar, M. P. Austeria, S. Sampath, Field effect transistor based on layered NiPS₃. Scient. Rep. 8, 8586 (2018).
- M. Tsurubayashi, K. Kodama, M. Kano, K. Ishigaki, Y. Uwatoko, T. Watanabe, K. Takase, Y. Takano, Metal-insulator transition in Mott-insulator FePS₃. AIP Adv. 8, 101307 (2018).
- D. G. Chica, Y. He, K. M. McCall, D. Y. Chung, R. O. Pak, G. Trimarchi, Z. Liu, P. M. De Lurgio, B. W. Wessels, M. G. Kanatzidis, Direct thermal neutron detection by the 2D semiconductor ⁶LilnP₂Se₆. Nature 577, 346–349 (2020).

- Y. He, I. Hadar, M. G. Kanatzidis, Detecting ionizing radiation using halide perovskite semiconductors processed through solution and alternative methods. *Nat. Photonics* 16, 14–26 (2022).
- M. A. Gave, D. Bilc, S. D. Mahanti, J. D. Breshears, M. G. Kanatzidis, On the lamellar compounds CuBiP₂Se₆, AgBiP₂Se₆ and AgBiP₂S₆. Antiferroelectric phase transitions due to cooperative Cu⁺ and Bi³⁺ Ion motion. *Inorg. Chem.* 44, 5293–5303 (2005).
- M. A. Susner, M. Chyasnavichyus, M. A. McGuire, P. Ganesh, P. Maksymovych, Metal thio- and selenophosphates as multifunctional van der Waals layered materials. Adv. Mater. 29, adma.201602852 (2017).
- J. S. O. Evans, D. O'Hare, R. Clement, A. Leaustic, P. Thuéry, Origins of the spontaneous magnetization in MnPS₃ intercalates: A magnetic susceptibility and powder neutron diffraction Study. *Adv. Mater.* 7, 735–739 (1995).
- P. A. Joy, S. Vasudevan, Magnetism in the layered transition-metal thiophosphates MPS₃ (M=Mn, Fe, and Ni). *Phys. Rev. B* 46, 5425–5433 (1992).
- X. Li, X. Wu, J. Yang, Half-metallicity in MnPSe₃ exfoliated nanosheet with carrier doping. J. Am. Chem. Soc. 136, 11065–11069 (2014).
- Y. Li, D. J. Singh, Properties of the ferroelectric visible light absorbing semiconductors: Sn₂P₂S₆ and Sn₂P₂Se₆. Phy. Rev. Mater. 1, 075402 (2017).
- X. Wang, J. Cao, Z. Lu, A. Cohen, H. Kitadai, T. Li, Q. Tan, M. Wilson, C. H. Lui, D. Smirnov,
 S. Sharifzadeh, X. Ling, Spin-induced linear polarization of photoluminescence in antiferromagnetic van der Waals crystals. *Nat. Mater.* 20, 964–970 (2021).
- T. Matsuoka, A. Haglund, R. Xue, J. S. Smith, M. Lang, A. M. dos Santos, D. Mandrus, Pressure-induced insulator–metal transition in two-dimensional Mott insulator NiPS₃. J. Physical Soc. Japan 90, 124706 (2021).
- J. He, S. H. Lee, F. Naccarato, G. Brunin, R. Zu, Y. Wang, L. Miao, H. Wang, N. Alem, G. Hautier, G.-M. Rignanese, Z. Mao, V. Gopalan, SnP₂S₆: A promising infrared nonlinear optical crystal with strong nonresonant second harmonic generation and phasematchability. ACS Photonics 9, 1724–1732 (2022).
- Z. Wang, R. D. Willett, R. A. Laitinen, D. A. Cleary, Synthesis and crystal structure of SnP₂S₆. Chem. Mater. 7, 856–858 (1995).
- P. S. Brody, High voltage photovoltaic effect in barium titanate and lead titanate-lead zirconate ceramics. J. Solid State Chem. 12, 193–200 (1975).
- G. B. Osterhoudt, L. K. Diebel, M. J. Gray, X. Yang, J. Stanco, X. Huang, B. Shen, N. Ni, P. J. W. Moll, Y. Ran, K. S. Burch, Colossal mid-infrared bulk photovoltaic effect in a type-l Weyl semimetal. *Nat. Mater.* 18, 471–475 (2019).
- Y. Jing, Z. Zhou, J. Zhang, C. Huang, Y. Li, F. Wang, SnP₂S₆ monolayer: A promising 2D semiconductor for photocatalytic water splitting. *Phys. Chem. Chem. Phys.* 21, 21064–21069 (2019).
- M. Lin, P. Liu, M. Wu, Y. Cheng, H. Liu, K. Cho, W.-H. Wang, F. Lu, Two-dimensional nanoporous metal chalcogenophosphates MP₂X₆ with high electron mobilities. *Appl. Sur. Sci.* 493, 1334–1339 (2019).
- 34. H. Peelaers, C. G. Van de Walle, Effects of strain on band structure and effective masses in MoS₂. *Phys. Rev. B* **86**, 241401 (2012).
- I. P. Studenyak, V. V. Mitrovcij, G. S. Kovacs, O. A. Mykajlo, M. I. Gurzan, Y. M. Vysochanskii, Temperature variation of optical absorption edge in Sn₂P₂S₆ and SnP₂S₆ crystals. Ferroelectrics 254, 295–310 (2001).
- P. Tonndorf, R. Schmidt, P. Böttger, X. Zhang, J. Börner, A. Liebig, M. Albrecht, C. Kloc,
 O. Gordan, D. R. T. Zahn, S. Michaelis de Vasconcellos, R. Bratschitsch, Photoluminescence emission and Raman response of monolayer MoS₂, MoSe₂, and WSe₂. Opt. Exp. 21, 4908–4916 (2013).
- 37. J. I. Pankove, Optical Processes in Semiconductors (Prentice Hall, 1971).
- C.-Y. Zhu, Z. Zhang, J.-K. Qin, Z. Wang, C. Wang, P. Miao, Y. Liu, P.-Y. Huang, Y. Zhang, K. Xu, L. Zhen, Y. Chai, C.-Y. Xu, Two-dimensional semiconducting SnP₂Se₆ with giant second-harmonic-generation for monolithic on-chip electronic-photonic integration. *Nat. Commun.* 14, 2521 (2023).
- S. A. Denev, T.T. A. Lummen, E. Barnes, A. Kumar, V. Gopalan, Probing ferroelectrics using optical second harmonic generation. J. Amer. Cer. Soc. 94, 2699–2727 (2011).
- 40. R. H. Bube, Photoelectronic Properties of Semiconductors (Cambridge Univ. Press, 1992).
- J. Kang, S. A. Wells, V. K. Sangwan, D. Lam, X. Liu, J. Luxa, Z. Sofer, M. C. Hersam, Solution-based processing of optoelectronically active indium selenide. *Adv. Mater.* 30, e1802990 (2018).
- M. Malik, M. A. Iqbal, J. R. Choi, P. V. Pham, 2D materials for efficient photodetection: Overview, mechanisms, performance and UV-IR range applications. Front. Chem. 10, 905404 (2022).
- C.-C. Wu, D. Jariwala, V. K. Sangwan, T. J. Marks, M. C. Hersam, L. J. Lauhon, Elucidating the photoresponse of ultrathin MoS₂ Field-Effect transistors by scanning photocurrent microscopy. J. Phys. Chem. Lett. 4, 2508–2513 (2013).
- M. Buscema, M. Barkelid, V. Zwiller, H. S. J. van der Zant, G. A. Steele,
 A. Castellanos-Gomez, Large and tunable photothermoelectric effect in single-layer MoS₂. Nano Lett. 13, 358–363 (2013).
- 45. M.-M. Yang, D. J. Kim, M. Alexe, Flexo-photovoltaic effect. Science 360, 904–907 (2018).
- Z. Liang, X. Zhou, L. Zhang, X.-L. Yu, Y. Lv, X. Song, Y. Zhou, H. Wang, S. Wang, T. Wang, P. P. Shum, Q. He, Y. Liu, C. Zhu, L. Wang, X. Chen, Strong bulk photovoltaic effect in

SCIENCE ADVANCES | RESEARCH ARTICLE

- engineered edge-embedded van der Waals structures. *Nat. Commun.* **14**, 4230 (2023).
- Q. Ma, C. H. Lui, J. C. W. Song, Y. Lin, J. F. Kong, Y. Cao, T. H. Dinh, N. L. Nair, W. Fang, K. Watanabe, T. Taniguchi, S.-Y. Xu, J. Kong, T. Palacios, N. Gedik, N. M. Gabor, P. Jarillo-Herrero, Giant intrinsic photoresponse in pristine graphene. *Nat. Nanotechnol.* 14, 145–150 (2019).
- Q. Ma, A. G. Grushin, K. S. Burch, Topology and geometry under the nonlinear electromagnetic spotlight. *Nat. Mater.* 20, 1601–1614 (2021).
- J. Tauc, Generation of an emf in semiconductors with nonequilibrium current carrier concentrations. Rev. Mod. Phys. 29, 308–324 (1957).
- Y. Gu, J. P. Romankiewicz, J. K. David, J. L. Lensch, L. J. Lauhon, Quantitative measurement of the electron and hole mobility—lifetime products in semiconductor nanowires. *Nano Lett.* 6, 948–952 (2006).
- Z. Xiao, Y. Yuan, Y. Shao, Q. Wang, Q. Dong, C. Bi, P. Sharma, A. Gruverman, J. Huang, Giant switchable photovoltaic effect in organometal trihalide perovskite devices. *Nat. Mater.* 14, 193–198 (2015).
- S.Y. Yang, J. Seidel, S. J. Byrnes, P. Shafer, C. H. Yang, M. D. Rossell, P. Yu, Y. H. Chu, J. F. Scott, J. W. Ager, L. W. Martin, R. Ramesh, Above-bandgap voltages from ferroelectric photovoltaic devices. *Nat. Nanotechnol.* 5, 143–147 (2010).
- X. Chen, K. Xu, T. Qin, Y. Wang, Y. Chen, H. Liu, Q. Xiong, Bulk photovoltaic effect in two-dimensional ferroelectric semiconductor alpha-ln₂Se₃. arXiv:2308.08382 [cond-mat. mtrl-sci] (21 August 2023).
- Y. Li, J. Fu, X. Mao, C. Chen, H. Liu, M. Gong, H. Zeng, Enhanced bulk photovoltaic effect in two-dimensional ferroelectric CulnP₂S₆. Nat. Commun. 12, 5896 (2021).
- C. F. Macrae, I. Sovago, S. J. Cottrell, P. T. A. Galek, P. McCabe, E. Pidcock, M. Platings, G. P. Shields, J. S. Stevens, M. Towler, P. A. Wood, Mercury 4.0: From visualization to analysis, design and prediction. *J. Appl. Crystal.* 53, 226–235 (2020).
- O.V. Dolomanov, L. J. Bourhis, R. J. Gildea, J. A. K. Howard, H. Puschmann, OLEX2: A complete structure solution, refinement and analysis program. J. Appl. Crystal. 42, 339–341 (2009).
- G. Sheldrick, Crystal structure refinement with SHELXL. Acta. Crystallogr. C Struct. Chem. 71. 3–8 (2015).
- M. Binnewies, R. Glaum, M. Schmidt, P. Schmidt, Transport of Selenides: In Chemical Vapor Transport Reactions (De Gruyter Inc, 2012).
- C. D. Carpentier, R. Nitsche, Vapour growth and crystal data of the thio(seleno)hypodiphosphates Sn₂P₂S₆, Sn₂P₂Se₆, Pb₂P₂Se₆ and their mixed crystals. MRS Bull. 9, 401–410 (1974)
- P. Makuła, M. Pacia, W. Macyk, How to correctly determine the band gap energy of modified semiconductor photocatalysts based on UV–Vis spectra. J. Phys. Chem. Lett. 9, 6814–6817 (2018).
- J. P. Perdew, K. Burke, M. Ernzerhof, Generalized gradient approximation made simple. Phys. Rev. Lett. 77, 3865–3868 (1996).
- G. Kresse, J. Furthmüller, Efficient iterative schemes for ab initiototal-energy calculations using a plane-wave basis set. Phys. Rev. B Condens. Matter. 54, 11169–11186 (1996).

- L. Z. Tan, F. Zheng, S. M. Young, F. Wang, S. Liu, A. M. Rappe, Shift current bulk photovoltaic effect in polar materials—hybrid and oxide perovskites and beyond. NPJ Comput. Mater. 2. 16026 (2016).
- D. C. Palmer, CrystalMaker. CrystalMaker Software Ltd, Begbroke, Oxfordshire, England. (2014)
- M. Nakamura, S. Horiuchi, F. Kagawa, N. Ogawa, T. Kurumaji, Y. Tokura, M. Kawasaki, Shift current photovoltaic effect in a ferroelectric charge-transfer complex. *Nat. Commun.* 8, 281 (2017)
- J. Ma, Q. Gu, Y. Liu, J. Lai, P. Yu, X. Zhuo, Z. Liu, J.-H. Chen, J. Feng, D. Sun, Nonlinear photoresponse of type-II Weyl semimetals. Nat. Mater. 18, 476–481 (2019).

Acknowledgments

Funding: This work was supported in part by the National Science Foundation through Grant DMR-2305731 (synthesis and material characterization) and DMR-1929356, V.K.S., T.T.C. L.J.L. and M.C.H. acknowledge support from the National Science Foundation Materials Research Science and Engineering Center at Northwestern University (NSF DMR-1720139 and DMR-2308691) for charge transport and photocurrent measurements. This work used the NUFAB and EPIC facilities of Northwestern University's NUANCE Center, which has received support from the SHyNE Resource (NSF Grant ECCS-2025633), Northwestern MRSEC program (NSF Grant DMR-2308691), the Keck Foundation, and the State of Illinois through IIN. J.H. and V.G. acknowledge support from the Air Force Office of Scientific Research Grant number FA 9550-23-1-0658. R.Z., J. S. and V.G. acknowledge support from the National Science Foundation grant number DMR-2210933. M.-A.K was supported by the Basic Science Research Program through the National Research Foundation of Korea (NRF) funded by the Ministry of Education (2021R1A6A3A14038611). Author contributions: V.K.S., D.G.C., and T.-T.C. wrote the manuscript with contributions from the other authors. D.G.C. and C.C.L. optimized the crystal growth and performed DTA experiments. D.G.C. and M.A.Q. collected SCXRD data and solved the structure, M.C., Y.L., and V.P.D. conducted TEM and STEM-EDS measurements, S.H. performed DFT calculations. E.Q. collected optical transmission spectra. R.Z., J.S., and J.H. conducted SHG measurements. H.C. performed PFM measurements. C.E.M. performed EBSD measurements. V.K.S. and M.-A.K. fabricated the SnP₂Se₆ devices and collected the AFM images, PL spectra, Raman spectra, and charge transport data. T.T.C., V.K.S., and L.J.L. performed and analyzed phototransistor and BPVE measurements. C.W., V.G., V.P.D., L.J.L., M.C.H., and M.G.K. supervised the project. Competing interests: The authors declare that they have no competing interests. Data and materials availability: All data needed to evaluate the conclusions in the paper are present in the paper and/or the Supplementary Materials.

Submitted 22 February 2024 Accepted 26 June 2024 Published 31 July 2024 10.1126/sciadv.ado8272